Electronic Supplementary Information for

Fe_2CS_2 MXene: a promising electrode for Al-ion batteries

Sangjin Lee,[a] Sung Chul Jung*[b] and Young-Kyu Han*[a]

[a]Department of Energy and Materials Engineering and Advanced Energy and Electronic Materials Research Center, Dongguk University-Seoul, Seoul 110-715, Republic of Korea

[b]Department of Physics, Pukyong National University, Busan 48513, Republic of Korea

*Corresponding Author

*E-mail: scjung@pknu.ac.kr and ykenergy@dongguk.edu

Computational details of MXene simulations

Spin-polarized density functional theory (DFT) calculations were carried out using the Vienna ab initio simulation package (VASP).[1] The projector augmented wave (PAW) method[2] and the van der Waals density functional (vdW-DF)[3–5] with the use of the optB86b exchange functional[3,6] were employed. The electronic wave functions were expanded in a plane wave basis set with 560 eV. The MXene phases were simulated using a periodic hexagonal supercell, including two MXene layers, with 2 × 2 and 3 × 3 surface unit cells. A 16 × 16 × 1 Γ-centered *k*-point mesh was used for the Brillouin zone integrations. The atomic geometry was optimized using a conjugate-gradient algorithm with the force convergence criterion of 0.005 eV $Å^{-1}$. The energy barriers for Al-ion diffusion in MXene were calculated using the climbing-image nudged elastic band (CINEB) method,[7] and the calculated barriers were used to evaluate the diffusivities at T = 300 K. A 2 × 2 surface unit cell, a 8 × 8 × 1 Γ-centered *k*-point mesh, and the force convergence criterion of 0.03 eV $Å^{-1}$ were used to perform the CINEB calculations. Our CINEB calculations were successfully applied to determine the energy barriers for the diffusions of the solvated Li, Na, and Mg ions in graphite[8,9] and the Na ions in graphite oxide.[10] Ab initio molecular dynamics (AIMD) simulations were used to examine the structural stability of the Fe_2CS_2 MXene at different temperatures. The equations of motion were integrated with the Verlet algorithm using a time step of 1 fs, and the temperature was controlled by velocity rescaling and canonical ensemble using a Nosé-Hoover thermostat. A 2 × 2 surface unit cell and a 2 × 2 × 1 Γ-centered *k*-point mesh were used during the AIMD simulations. The Fe_2CS_2 MXene structure was analyzed by calculating the radial distribution functions (RDFs) using the rigorous investigation of networks generated using simulations (RINGS) code.[11] All the structures were illustrated using the visualization for electronic and structural analysis (VESTA) program.[12]

Thermal stability of the Fe_2CS_2 MXene structure using AIMD simulations

Ab initio molecular dynamics (AIMD) simulations provided in the VASP code were performed to examine the thermal stability of the Fe_2CS_2 MXene at different temperatures of T = 300 K, 600 K, 900 K, 1200 K, 1500 K, 1800 K, and 2100 K. The equations of motion were integrated with the Verlet algorithm using a time step of 1 fs. The temperature was controlled by velocity rescaling and canonical ensemble using a Nosé-Hoover thermostat. The Fe_2CS_2 structures at different temperatures were simulated for 10 ps. The radial distribution functions (RDFs) of Fe_2CS_2 MXene at each temperature were calculated using RINGS code.[11] In addition to the RDFs for the Fe–C and Fe–S pairs (Fig. 2a), the RDFs for the Fe–Fe, C–C, and S–S pairs were presented in Fig. S1a, which clearly show that the ordered structure of Fe_2CS_2 MXene is maintained up to T = 900 K. In particular, the second peaks for the S–S pair rapidly collapse above T = 1200 K, indicating the Fe_2CS_2 structure starts to degrade from the surface termination group. This result is compatible with the RDFs for the Fe–C and Fe–S pairs in Fig. 2a, where the temperature at which the structural collapse is observed is lower for the Fe–S pair than the Fe–C pair. The maintenance of the ordered Fe_2CS_2 structure at T = 900 K is evidenced by the atomic structures at different temperatures, as shown in Fig. S1b.

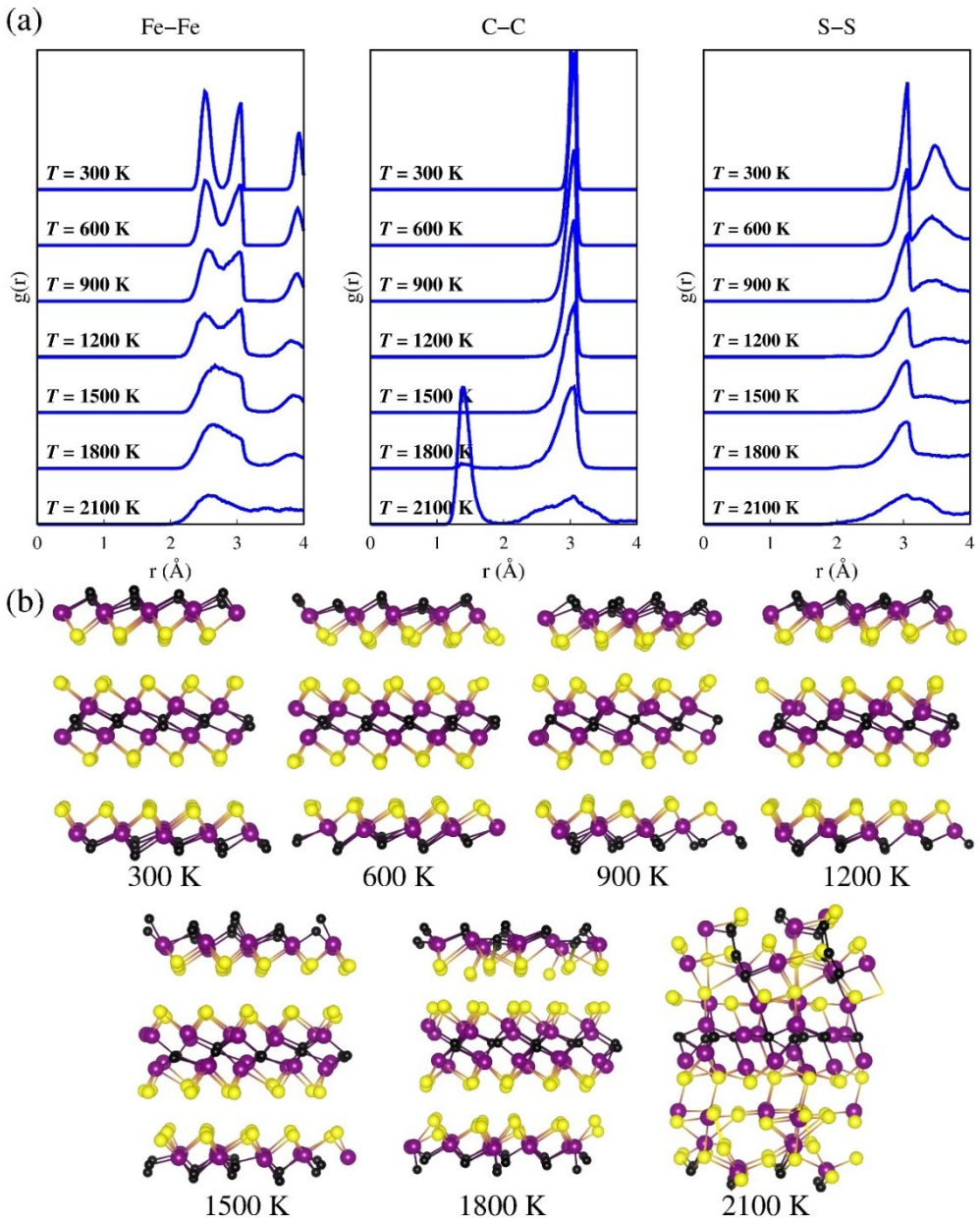

Fig. S1. (a) Partial radial distribution functions g(r) for the Fe–Fe, C–C, and S–S pairs in Fe_2CS_2 MXene, obtained from the AIMD simulations for 10 ps at T = 300 K, 600 K, 900 K, 1200 K, 1500 K, 1800 K, and 2100 K. (b) Structures of the Fe_2CS_2 MXene after the AIMD simulations for 10 ps. The yellow, purple, and black spheres represent the S, Fe, and C atoms, respectively.

Al-ion intercalation energies of $Al_xM_2CT_2$ MXenes

Intercalation energies of $Al_xM_2CT_2$ MXenes (M = Ti and Fe and T = O and S) were calculated at different Al concentrations of x = 0.11, 0.25, 0.5, 0.75, and 1.0 for Ti_2CO_2 and Ti_2CS_2 and x = 0.11, 0.25, 0.5, 0.75, 1.0, 1.5, and 2.0 for Fe_2CO_2 and Fe_2CS_2. The calculated MXenes structures were the same as those in previous studies,[13–15] where the transition metals (Ti and Fe) are in the hexagonal close packing (*hcp*) sites, and the C atoms are in the octahedral interstitial sites. For each Al concentration x in $Al_xFe_2CS_2$, several atomic structures were examined to determine the most stable $Al_xFe_2CS_2$ structure for all concentrations, as illustrated in Fig. S2 and S3. The determined most stable $Al_{1.5}Fe_2CS_2$ structure was displayed in Fig. S3. For $Al_xTi_2CO_2$, $Al_xTi_2CS_2$, and $Al_xFe_2CO_2$, the most stable structures were determined in the same way as in $Al_xFe_2CS_2$, and the determined structures were displayed in Fig. S4. All the atomic structures were plotted using the visualization for electronic and structural analysis (VESTA) program.[12]

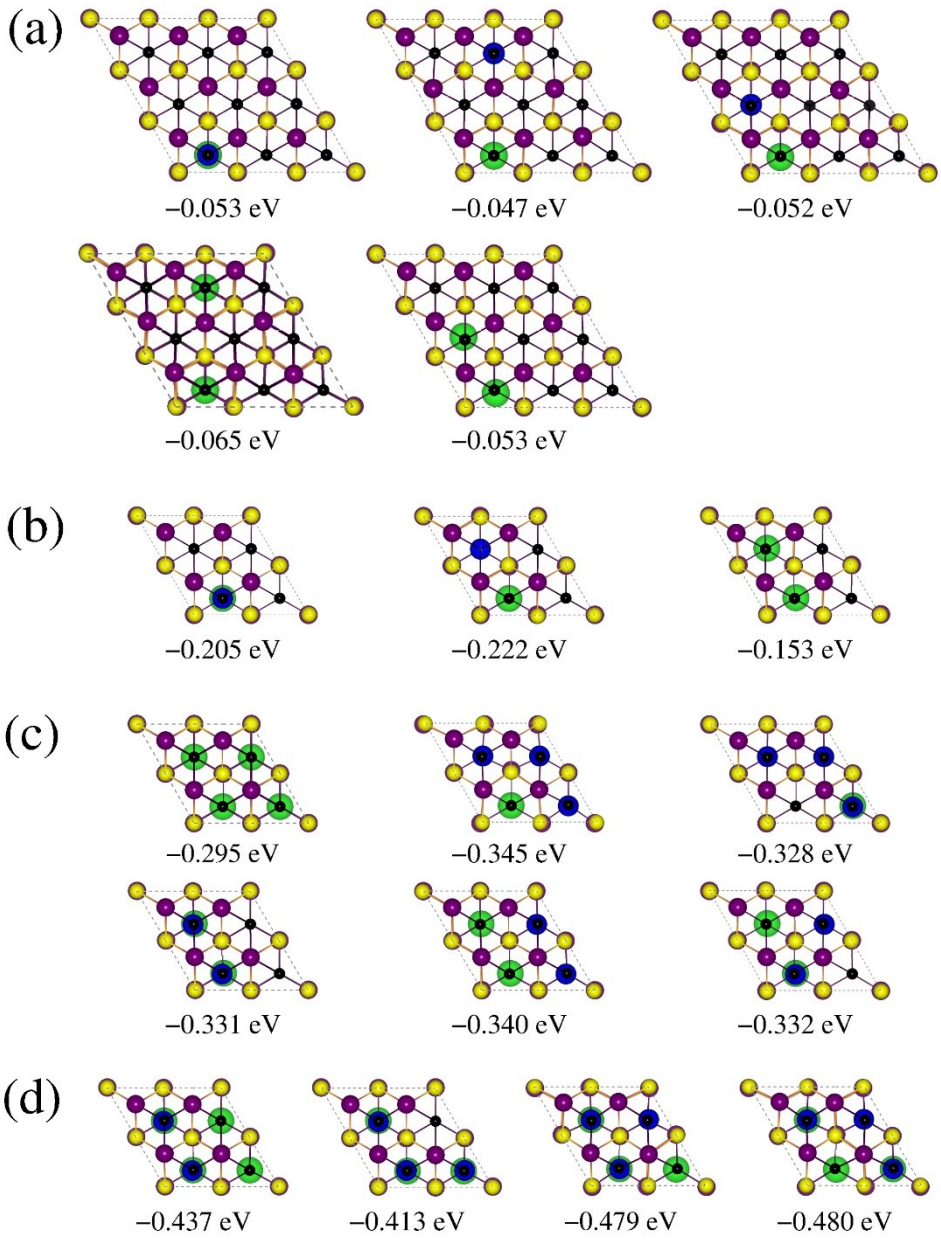

Fig. S2. Top views of $Al_xFe_2CS_2$ MXene structures at different Al concentrations: (a) x = 0.11, (b) x = 0.25, (c) x = 0.5, and (d) x = 0.75. The blue/green, yellow, purple, and black spheres represent Al, S, Fe, and C atoms, respectively. The blue and green spheres represent the Al atoms occupying the upper and lower ones of the two separate interlayer spaces in the unit cell, respectively. The numbers represent the calculated intercalation energies.

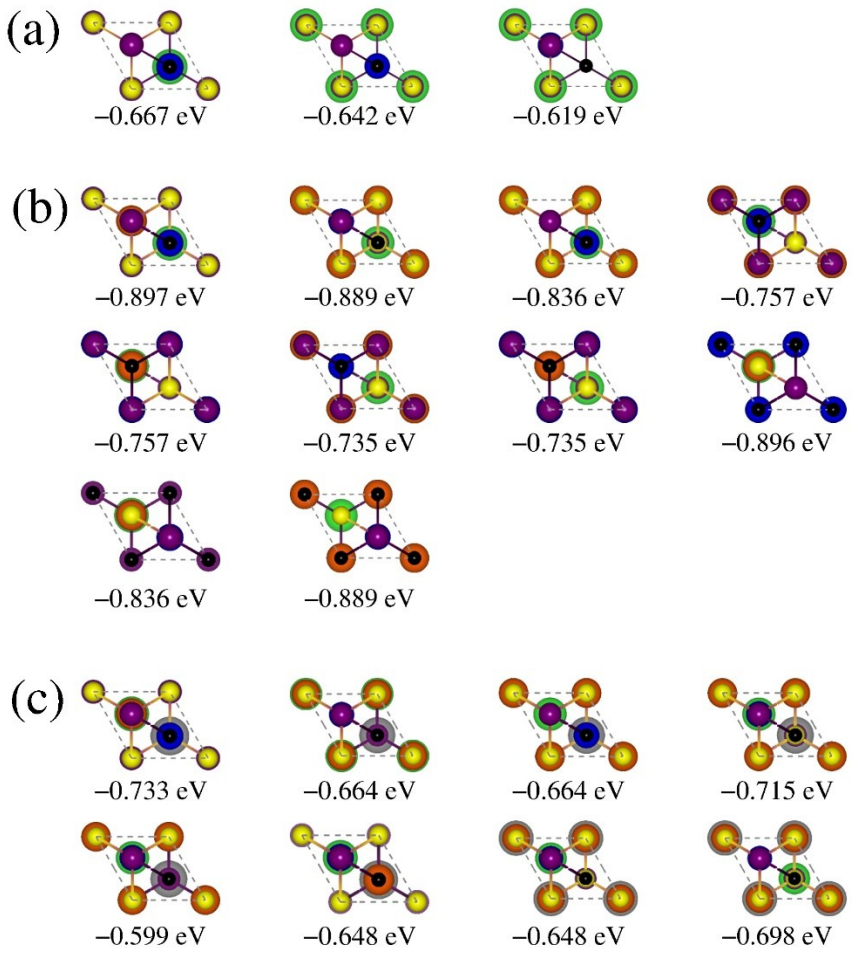

Fig. S3. Top views of $Al_xFe_2CS_2$ MXene structures at different Al concentrations: (a) x = 1.0, (b) x = 1.5, and (c) x = 2.0. The blue/orange/green/grey, yellow, purple, and black spheres represent Al, S, Fe, and C atoms, respectively. The blue/orange and green/grey spheres represent the Al atoms occupying the upper and lower ones of the two separate interlayer spaces in the unit cell, respectively. The vertical positions of the Al atoms increase in the order of grey < green < orange < blue. The numbers represent the calculated intercalation energies.

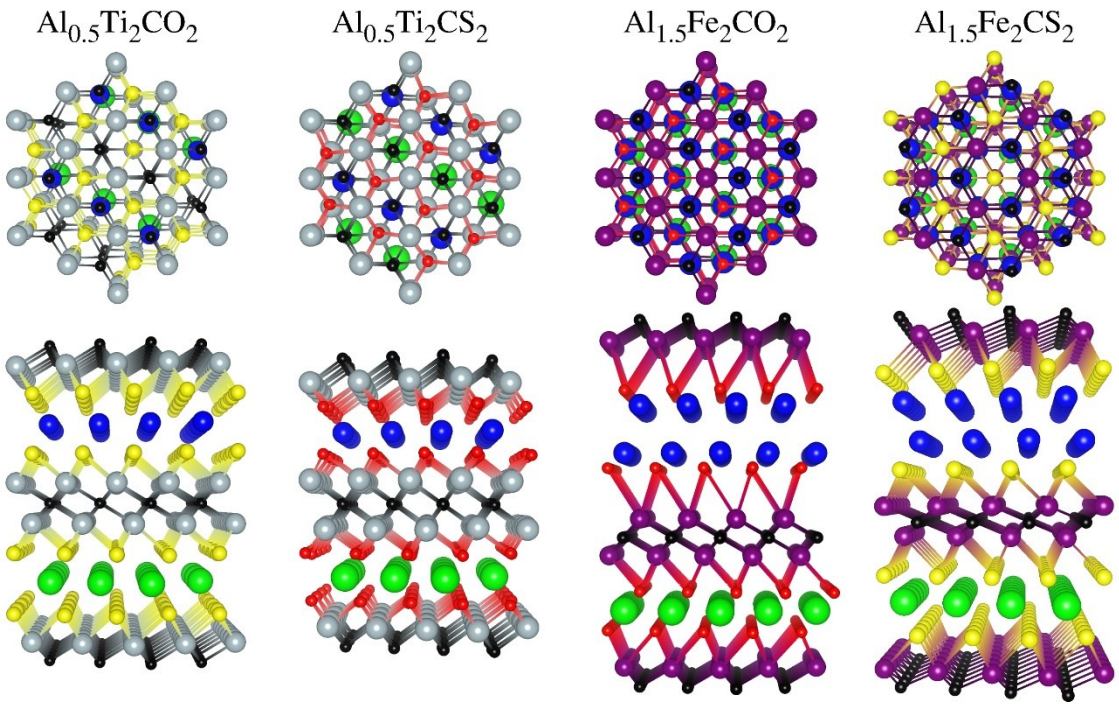

Fig. S4. Top views (upper) and side views (lower) of the most stable $Al_{0.5}Ti_2CO_2$, $Al_{0.5}Ti_2CS_2$, $Al_{1.5}Fe_2CO_2$, and $Al_{1.5}Fe_2CS_2$ structures. The blue/green, red, yellow, grey, purple, and black spheres represent Al, O, S, Ti, Fe, and C atoms, respectively. In the side views, the Al atoms in the upper and lower interlayer spaces are denoted by blue and green, respectively, for clarity.

Charges of transition metals and surface termination groups in MXenes

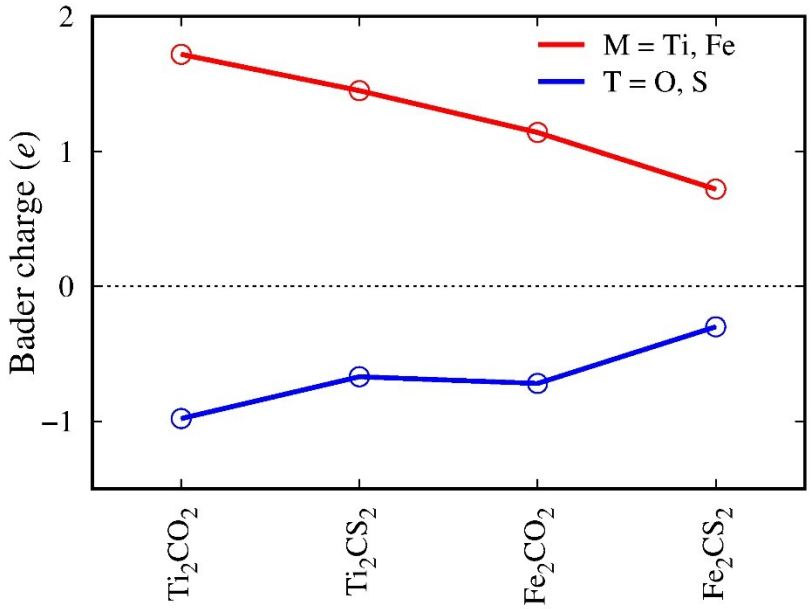

Fig. S5. Bader charges of M and T atoms in M_2CT_2 MXene, where M = Ti and Fe and T = O and S.

MXene properties for Ai-ion batteries

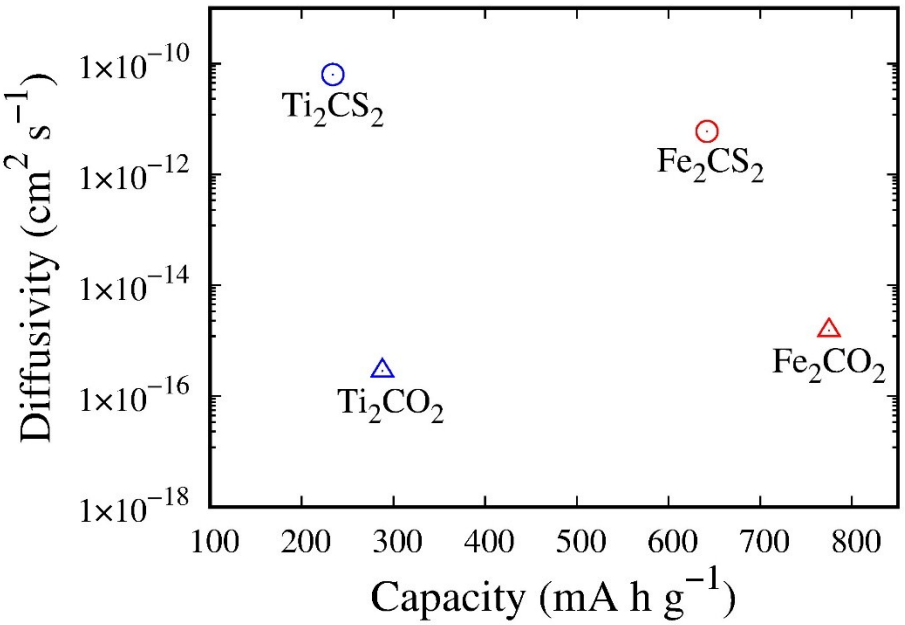

Fig. S6. Specific capacities and Al ion diffusivities of Ti_2CO_2, Ti_2CS_2, Fe_2CO_2, and Fe_2CS_2 MXenes for Al-ion batteries.

Electronic structure of the Fe_2CS_2 MXene

The band structure and density of states of Fe_2CS_2 MXene were computed in order to examine the electronic structure of Fe_2CS_2. In order to precisely evaluate the band structures, we adopted Heyd-Scuseria-Ernzerhof (HSE06) hybrid functional[16] implemented in the VASP code. As shown in Fig. S7, while Ti_2CO_2 examined for comparison shows a band gap of 0.64 eV, Fe_2CS_2 shows a metallic band structure without a band gap, indicating a superior electronic conductivity of Fe_2CS_2 compared to Ti_2CO_2.

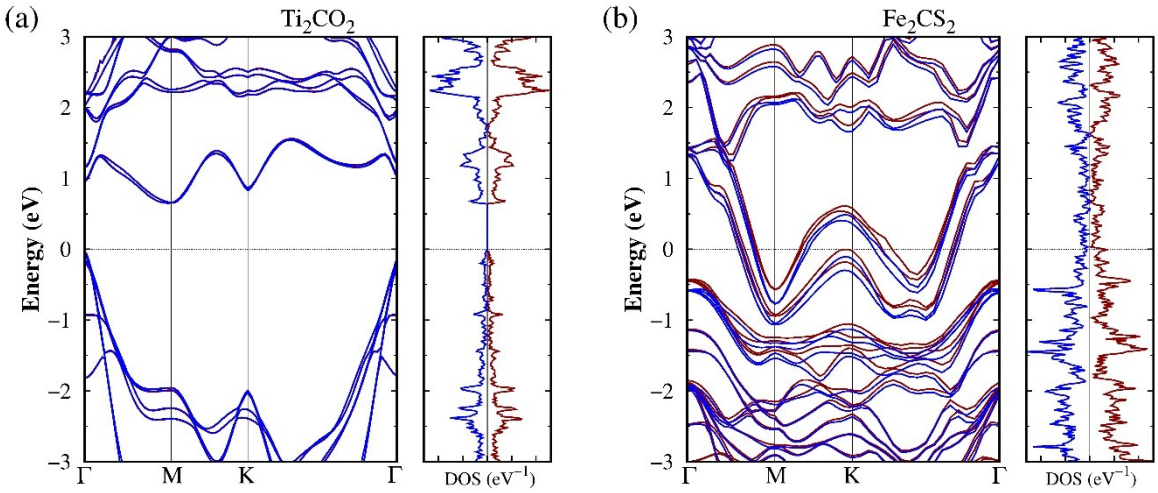

Fig. S7. Band structures and density of states of (a) Ti_2CO_2 and (b) Fe_2CS_2 MXenes. Blue and red lines represent the majority- and minority-spin states, respectively. Dashed lines represent the Fermi level.

Al-ion intercalation energies of hybrid MXenes

Intercalation energies of $Al_xFe_2TiC_2S_2$ and $Al_xFe_2Ti_2C_3S_2$ hybrid MXenes, including both early and late transition metals (Ti and Fe), were calculated at different Al concentrations of x = 0.25, 0.5, 0.75, 1.0, 1.5, and 2.0. As shown in Fig. S8a, the most stable compositions are $Al_{1.5}Fe_2TiCS_2$ and $Al_{1.5}Fe_2Ti_2C_3S_2$, with the intercalation energies of –1.35 eV and –1.46 eV, respectively. The corresponding specific capacities are 487 mA h g^{-1} and 392 mA h g^{-1}, respectively. The optimized $Al_{1.5}Fe_2TiCS_2$ and $Al_{1.5}Fe_2Ti_2C_3S_2$ structures have alternating monolayers and bilayers of intercalated Al ions, as shown in Fig. S8b.

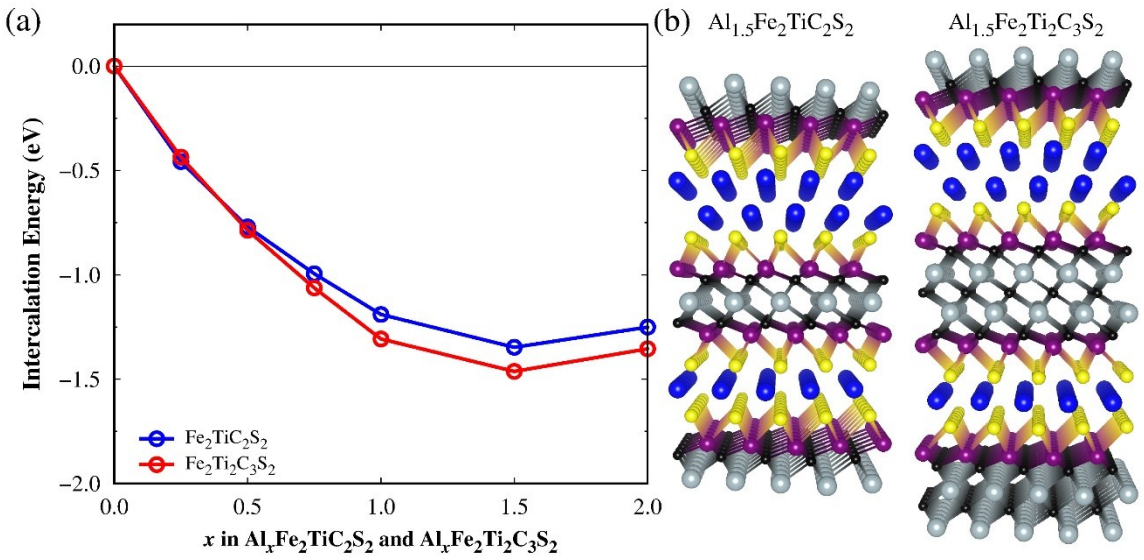

Fig. S8. (a) Intercalation energies of $Al_xFe_2Ti_nC_{n+1}S_2$ hybrid Mxenes (n = 1 and 2), defined as $E_{int} = E(Al_xFe_2Ti_nC_{n+1}S_2) - xE(Al) - E(Fe_2Ti_nC_{n+1}S_2)$, where $E(Al_xFe_2Ti_nC_{n+1}S_2)$ is the energy per $Al_xFe_2Ti_nC_{n+1}S_2$ unit, $E(Al)$ is the energy per atom of *fcc* Al crystal, and $E(Fe_2Ti_nC_{n+1}S_2)$ is the energy per $Fe_2Ti_nC_{n+1}S_2$ unit. (b) Structures of $Al_{1.5}Fe_2Ti_nC_{n+1}S_2$ MXenes. The blue, yellow, purple, grey and black spheres represent the Al, S, Fe, Ti, and C atoms, respectively.

References

1 G. Kresse and J. Furthmüller, *Phys. Rev. B*, 1996, **54**, 11169–11186.

2 P. E. Blöchl, *Phys. Rev. B*, 1994, **50**, 17953–17979.

3 J. Klime, D. R. Bowler and A. Michaelides, *Phys. Rev. B*, 2011, **83**, 195131.

4 M. Dion, H. Rydberg, E. Schröder, D. C. Langreth and B. I. Lundqvist, *Phys. Rev. Lett.*, 2004, **92**, 22–25.

5 G. Román-Pérez and J. M. Soler, *Phys. Rev. Lett.*, 2009, **103**, 096102.

6 J. Klimes, D. R. Bowler and A. Michaelides, *J. Phys. Condens. Matter*, 2010, **22**, 022201.

7 G. Henkelman, B. P. Uberuaga, H. Jónsson and G. Henkelman, *J. Chem. Phys.*, 2011, **113**, 9901.

8 S. C. Jung, Y. J. Kang and Y.-K. Han, *Nano Energy*, 2017, **34**, 456–462.

9 D. M. Kim, S. C. Jung, S. Ha, Y. Kim, Y. Park, J. H. Ryu, Y.-K. Han and K. T. Lee, *Chem. Mater.*, 2018, **30**, 3199–3203.

10 Y.-J. Kang, S. C. Jung, J. W. Choi and Y.-K. Han, *Chem. Mater.*, 2015, **27**, 5402–5406.

11 S. Le Roux and P. Jund, *Comput. Mater. Sci.*, 2010, **49**, 70–83.

12 K. Momma and F. Izumi, *J. Appl. Crystallogr.*, 2011, **44**, 1272–1276.

13 H. W. Wang, M. Naguib, K. Page, D. J. Wesolowski and Y. Gogotsi, *Chem. Mater.*, 2016, **28**, 349–359.

14 C. Shi, M. Beidaghi, M. Naguib, O. Mashtalir, Y. Gogotsi and S. J. L. Billinge, *Phys. Rev. Lett.*, 2013, **112**, 125501.

15 M. Naguib, O. Mashtalir, J. Carle, V. Presser, J. Lu, L. Hultman, Y. Gogotsi and M. W. Barsoum, *ACS Nano*, 2012, **6**, 1322–1331.

16 A. V. Krukau, O. A. Vydrov, A. F. Izmaylov and G. E. Scuseria, *J. Chem. Phys.*, 2006, **125**, 224106.